Drying with Formation of Capillary Rings in a Model Porous Medium

Nicole Vorhauer, Y.J. Wang, Abdolreza Karaghani, Evangelos Tsotsas, Marc Prat

DOI 10.1007/s11242-015-0538-1

Drying with Formation of Capillary Rings in a Model Porous Medium

N. Vorhauer[1] · Y. J. Wang[1] · A. Kharaghani[1] · E. Tsotsas[1] · M. Prat[2,3]

Abstract Modelling of drying processes without adjustable parameters is still a challenge. As emphasized in several previous works, this might partly be due to the impact of liquid films trapped in corners of the pore space. In this study, we present and analyse a drying experiment with a micromodel, which clearly shows the presence of corner films. In contrast with previous works, however, the corner films do not form a system of interconnected corner films extending over large regions in our micromodel. They rather form isolated capillary rings surrounding the solid blocks of the device, and thus, a quasi-two-dimensional version of liquid bridges often observed in the contact regions between grains in soils and packings of particles. These capillary rings essentially remain confined in the two-phase region. As a result, their impact on drying rate is much smaller than in systems favouring films hydraulically connected over long distances. The capillary liquid ring formation is taken into account in a pore network model of drying leading to satisfactory agreement with the experiment provided that the lateral pinning of liquid phase observed in the experiment is included in the model. Based on this, the model enriches the family of pore network models of drying and can be considered as a step towards the modelling of secondary capillary effects in drying in more complex geometry.

Keywords Drying · Micromodel · Pore network model · Capillary rings

✉ N. Vorhauer
nicole.vorhauer@ovgu.de

1 Otto-von-Guericke University Magdeburg, Universitaetsplatz 2, 39106 Magdeburg, Germany

2 INPT, UPS, IMFT (Institut de Mécanique des Fluides de Toulouse), Université de Toulouse, 6 Allée Emile Monso, 31400 Toulouse, France

3 CNRS, IMFT, Allée du Professeur Camille Soula, 31400 Toulouse, France

List of symbols

$A_{\mathrm{i,tot}}$	Total evaporation surface area (m^2)
A_{t}	Cross-sectional area of throats (m^2)
A_{r}	Ring evaporation surface area (m^2)
h	Film height (m)
L	Lattice spacing (m)
L_{r}	Ring width (m)
L_{d}	Network depth (m)
$\tilde{M}$	Molar mass ($\mathrm{kg\ kmol}^{-1}$)
$\dot{M}$	Mass flow rate ($\mathrm{kg\ s}^{-1}$)
P	Total pressure (Pa)
P_{c}	Capillary pressure (Pa)
P_{l}	Liquid pressure (Pa)
P_{v}	Vapour pressure (Pa)
P_{v}^*	Saturation vapour pressure (Pa)
$P_{\mathrm{v},\infty}$	Vapour pressure in the bulk air phase (Pa)
r_{t}	Throat radius (m)
$\bar{r}_{\mathrm{t}}$	Mean throat radius (m)
$r_{\mathrm{t,d}}$	Meniscus radius at ring detachment (m)
$\tilde{R}$	Universal gas constant ($\mathrm{kJ\ kmol}^{-1}\ \mathrm{K}^{-1}$)
s_{BL}	Boundary layer thickness (m)
S	Total network saturation (–)
t	Time (s)
T	Temperature (°C)
$\bar{T}$	Mean temperature (°C)
V	Volume (m^3)

Greek symbols

α	Fitting parameter (–)
δ	Diffusivity ($\mathrm{m}^2\ \mathrm{s}^{-1}$)
θ	Contact angle (–)
σ	Surface tension ($\mathrm{N\,m}^{-1}$)

Subscripts

0	Initial value
∞	Bulk phase
i, j, k, l	Pore indices, ring indices
ij, kl, ik, jl, mk	Throat indices
p	Pore
t	Throat
r	Ring
v	Vapour

1 Introduction

Although many studies have been devoted to the drying of porous media, even the simplest situations, for example the slow drying of a packing of particles, are still a subject of investigation. In brief, predicting the transition between stage 1 (the period of fastest evaporation) and stage 2 (characterized by a significant decrease in the evaporation rate) or more simply the time needed to reach a given saturation during stage 2 is still challenging. One possible reason for this situation is the effect of secondary capillary trapping of the liquid phase in geometrical singularities of the pore space such as wedges, corners, crevices, roughness, contact regions between grains. This trapping can occur in regions invaded by the gas phase. The classical picture is to consider that the liquid phase can still be present in pores already invaded by the gas phase as a result of drying. In such a pore, the gas phase occupies the central part of the pore, whereas the liquid is present in the aforementioned singularities of the pore. The simplest situation of this type is the evaporation in a square tube where the corner capillary films can lead to evaporation kinetics an order of magnitude faster than in a circular tube, e.g. Chauvet et al. (2009). Also, it has been shown, e.g. Chauvet et al. (2010), that geometrical details, such as the degree of roundedness of the internal corners in a square tube, could have a major impact on the stage 1–stage 2 transition (which is also observed with a square tube). Similar strong effects of capillary films have also been observed in packings of spheres confined between two plates (Yiotis et al. 2012). The geometrical structure of capillary films in random packings of particles such as the ones considered by Yiotis et al. (2012) is of course much more complex, e.g. Geoffroy and Prat (2014), than the strait corner films in a square tube (as described by Chauvet et al. (2009)). If the film geometry is furthermore very sensitive to geometrical details as discussed, the drying model and analysis should be accessed by accounting for the film effect description. However, the situation in classical 3D packings of particles, i.e. not confined between two plates as in Yiotis et al. (2012), and more generally in real porous media is still somewhat unclear. Although X-ray tomography images clearly show the presence of pendular rings, e.g. Wang et al. (2013, 2014), as well as a zoology of complex ramified liquid structures, e.g. Scheel et al. (2008), it is difficult to conclude that these structures form a hydraulically well-connected system over long distances (= many pore sizes) in drying.

In summary, two main situations can be distinguished regarding the formation of secondary capillary structures: systems where these structures develop over a macroscopic region and have a huge impact on drying and systems where the dominant secondary capillary structures are of much smaller spatial extension. Tubes of polygonal cross section and the system considered by Yiotis et al. (2012) are examples of the first category, whereas it is still unclear whether a fully 3D random packing of particles belongs to the first or second category. Although it would thus be highly desirable to investigate further what happens in real porous media regarding the possible influence of secondary capillary effects on drying, we think that the consideration of a simpler system can be a useful step. As noted in Scheel et al. (2008), the geometrical complexity of the secondary capillary structures can be quite high in real porous media and thus difficult to characterize, whereas the consideration of a simpler system can provide insights into the formation of capillary structures and their impact on drying much easier. Based on this brief review of the literature, the objective of the present article was thus to study drying in a system leading to the formation of secondary capillary structures not connected over a long distance. These structures will be referred to as capillary rings. According to the two situations distinguished above, this system thus belongs to the second category, i.e. the less studied category. To the best of our knowledge, Wang et al. (2013, 2014)

and Mahmood (2013) were the first who proposed a liquid ring model for drying of a cubic regular pore network based on their experimental findings during drying of irregularly packed beads. Wang et al. (2013, 2014) found that pendular liquid rings can remain around each contact point of the glass beads when the main liquid phase recedes maintaining a generally high interconnection of the liquid phase inside the glass bead packing.

As in many previous works on two-phase flows in porous media, e.g. Lenormand et al. (1983), Lenormand and Zarcone (1984), Laurindo and Prat (1996, 1998), Tsimpanogiannis et al. (1999), Yiotis et al. (2012), the system we consider is a micromodel, i.e. a quasi-two-dimensional system of interconnected channels. The main advantage of this type of system is to permit the direct visualization of phase distributions using a simple camera. Interesting additional information will be obtained, however, using confocal laser scanning microscopy. The phenomenology of drying, derived from the experiment, will be used to develop a pore network model of drying with capillary ring formation. Then a parametric study will be performed in order to assess the impact of the capillary rings and their dynamics. As we shall see, the pore network model with capillary rings overpredicts the drying time compared to the experiment. This is explained by edge effects leading to the pinning of evaporation front on lateral edges of the pore network micromodel.

To conclude this introduction, we note that studies of drying based on pore network models (PNM) are now quite numerous, see e.g. the review articles Prat (2002, 2011) and the book chapter Metzger et al. (2007) and references therein. The novel model presented here accounts for capillary rings, similarly as in Wang et al. (2013, 2014), but in relation with a much simpler situation. We consider a quasi-two-dimensional system of channels which is opposed to the random packing of particles studied by Wang et al. (2013, 2014), and furthermore, we present the comparison of simulated results with the results of a drying experiment (which is lacking for the 3D system).

2 Experiments

2.1 Drying with Secondary Capillary Effects

Experiments were conducted in 2D square pore networks containing 50×50 pores with one open side, corresponding to the top side in the figures of the article.

Figure 1 sketches a detail of the micromodel geometry at pore scale. The channels are referred to as throats, and the nodes are denoted as the pores. The micromodel networks were produced by photolithography followed by isotropic wet etching of silicon dioxide (SiO_2). Afterwards, the glass structure was sealed by chemical bonding to a silicon (Si) wafer. The etching rate is independent of direction in the isotropic wet etching process allowing a throat geometry as illustrated in Fig. 2, which sketches the cross section of throats. As can be seen, the throats are half cylindrical with two sharp corners. Width of the pore throats obeys a Gaussian distribution with mean 164 μm and standard deviation 15 μm. Distance between the centre of two pores is uniform, $L = 1000\,\mu$m; and throats have uniform depth of $L_d = 39\,\mu$m. The saturation of network with liquid before the start of drying experiments was conducted in a liquid-filled vacuum chamber. For this, we placed the network in a liquid bath inside the vacuum chamber. When the pressure inside the chamber was reduced in the first step, the network channels evacuated completely, with $P \to 0$ inside the network channels. When the pressure was again slowly increased in the second step, the network channels were invaded with liquid. With this method, more than 99.5 % of the throats could

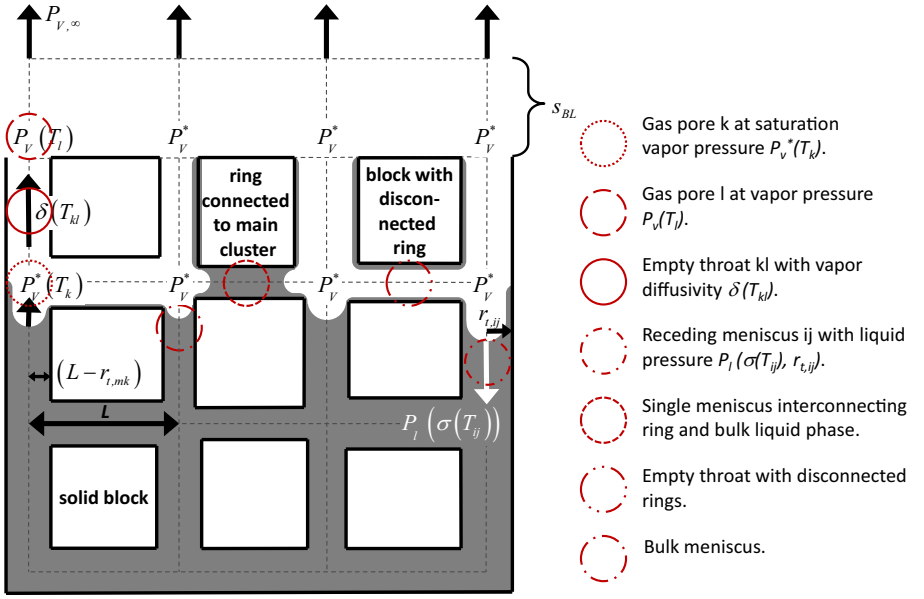

Fig. 1 Top view of an illustrative pore network of size 4×4 pores with discretized boundary layer of thickness s_{BL}, detailing pores, channels (throats), solid blocks, bulk menisci, single menisci. A capillary liquid ring detached from a liquid cluster is shown as well as a ring attached to a liquid cluster. Liquid in *grey*. Gas phase and solid blocks in *white*

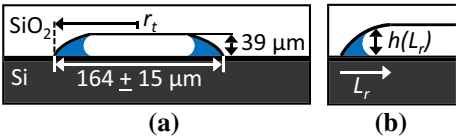

Fig. 2 **a** Channel cross section with sketch of capillary liquid films (in *blue*) trapped in the corners, **b** a corner partially occupied by liquid (in *blue*) with the notations used in Sect. 3.2.2

be filled with deionized water (0.5 % of the throats remained gas filled). Note that monitoring of the drying experiment started with some delay, i.e. when the overall network saturation already decreased to $S_0 = 0.94$.

The drying experiment was performed under quasi-isothermal conditions ($T \approx 63\,^{\circ}\mathrm{C}$). See Vorhauer et al. (2013, 2014) for more details. As expected from previous works and illustrated in Fig. 3, drying under these conditions leads to invasion percolation patterns with progressive evaporation of the liquid clusters forming as a result of the capillarity-controlled invasion.

In addition, the close inspection of the drying process in experiments shows that apparently empty channels temporarily possess an intermediate grey value that disappears when drying proceeds. From similar observations in previous works, e.g. Laurindo and Prat (1998), these grey variations are attributed to the drying of capillary corner films. Thus, a rapid conclusion would be that the situation is similar to the ones discussed in Laurindo and Prat (1998) and Prat (2007). We claim, however, that the situation in the present experiment is fundamentally different from the ones considered in Laurindo and Prat (1998) or Prat (2007). The difference lies in the hydraulic continuity of the corner films. In the micromodel used by Laurindo and Prat (1998), the films are continuous, i.e. they can extend over a region containing numerous pores or grains (blocks if we refer to the geometry of our experimental network). The long

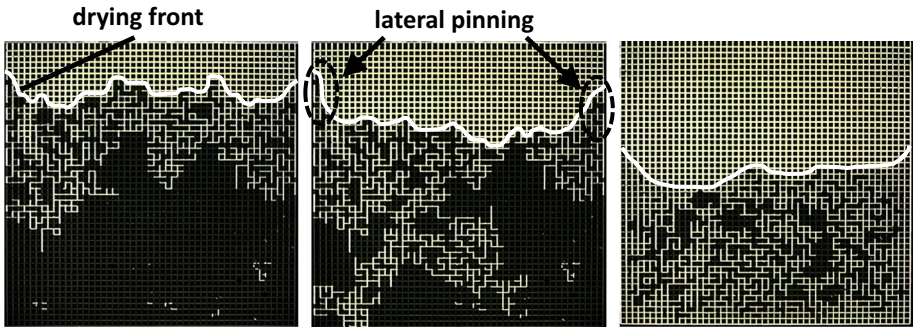

Fig. 3 Experimental images of phase distribution during the drying process. Three regions can be distinguished: dry zone (*white channels*), liquid regions (in *black*) and regions of intermediate *grey* values where liquid is present in the channel corners. The *white line* approximately indicates the position of the evaporation front. The *dashed circles* materialize the edge effect (pinning of liquid phase along the lateral edges) discussed in the paper (see Sect. 5.3)

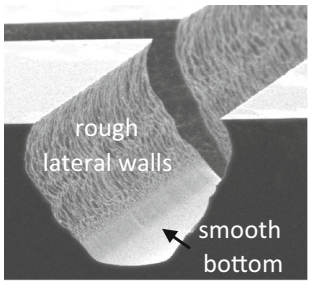

Fig. 4 Cross section of open SiO_2 pore network wafer. The channel bottom is smooth

distance transport within the films in their micromodel is possible due to the roughness of the pore walls, especially the roughness of the channel bottom and top walls, see also Lenormand et al. (1983) and Lenormand and Zarcone (1984). As illustrated in Fig. 4, which shows the cross section of the pore network etched in the SiO_2 wafer, these walls are actually smooth in our silicon-glass micromodel. This is a major difference compared to the resin micromodel used in Laurindo and Prat (1998), where the bottom wall was rough. As can be seen from Fig. 4, indeed the laterally etched channel walls clearly exhibit a higher roughness than the channel bottom (and the top wall, which is not visible in Fig. 4). This is due to the etching process.

Thin wetting films, if any, might exist over the smooth channel top and bottom surfaces in our micromodel, but they would be much too thin to ensure the hydraulic conductivity of the film regions. Thus, in contrast with the situation analysed in Laurindo and Prat (1998) or Prat (2007), in our pore network, the hydraulic connectivity of the film is on the order of one block size. Under these circumstances, the spatial organization of corner films must be fundamentally different than the one considered in previous works on pore network modelling of drying with films, e.g. Yiotis et al. (2003, 2004) and Prat (2007), i.e. discrete corner films located around blocks without hydraulic connection between these blocks. This is opposed to a continuous system of films extending over many pores (blocks).

To continue in this direction, it is therefore important to further characterize the films forming in our experiment, which is the objective of the next subsection.

2.2 Confocal Laser Scanning Microscopy

In order to gain precise information about the film region and film properties, drying of pore network has been investigated using confocal laser scanning microscopy (CLSM) (Leica TCS SPE, 10× magnification, red laser 635 nm). CLSM has the advantage of very high resolution (2048 × 2048 pixels, 96 dpi), depth of sharpness and contrast, which is obtained from pointwise scanning of the sample with a focused laser beam and additional digitalizing of the information (plus high frame rate). Usual applications are based on laser-induced fluorescence, whereas our research was limited to application of ordinary light refraction. Furthermore, in the first attempt, we focused on the top view of liquid phase (a full 3D scan of the network including films will be the subject of a future investigation). A sequence of pore and throat emptying with development of liquid films along lateral walls of the channels is shown in Fig. 5. The image sequence has been obtained from CLSM with the lowest magnification. Figure 5 shows one pore junction together with the neighbouring throats. Drying of a film is signified by growth of the black flanks of channels (which are related to the rougher surface as explained in the previous section) in Fig. 5. In Fig. 5a, throats to the north, east and south of the pore junction as well as the pore itself are completely saturated with liquid. The junction is invaded by the non-wetting phase in the throat to the west; the phase boundary between gas and liquid phase is located at the concave bulk meniscus in this throat. Furthermore, liquid remains inside the top and bottom edges of the horizontal channel (identifiable as thin grey films). Progressive emptying of neighbouring throats as well as the pore (with liquid remaining inside edges) is shown in Fig. 5b–d, additionally indicating the formation of an interconnecting liquid bridge that is found inside the western throat of the junction and that connects the facing liquid films. A magnification of Fig. 5f is given in

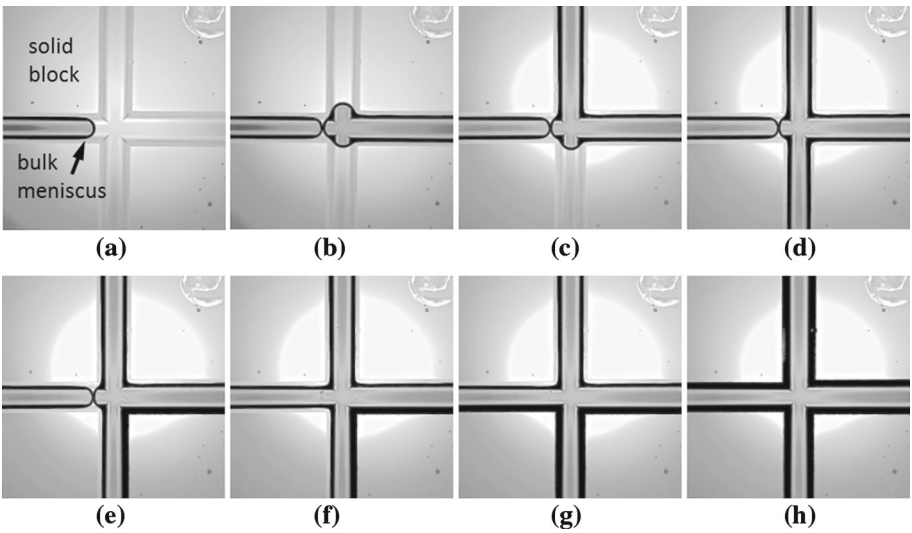

Fig. 5 CLSM images prove the existence of disconnected liquid film rings inside channel edges (identifiable as thin grey films) during drying of the pore network. **a** Emptying of the west throat, **b** emptying of the east throat and the pore, with a liquid meniscus already receding into the north throat as well as a liquid bridge forming inside the west throat, **c** emptying of the north throat, **d** emptying of the south throat, **e** drying of the south-east ring, **f** disconnection of south-west and north-west ring (disappearance of liquid bridge), **g** drying of south-east ring, **h** all rings dry. View is from the *top*

Fig. 6 Emphasis of film rings

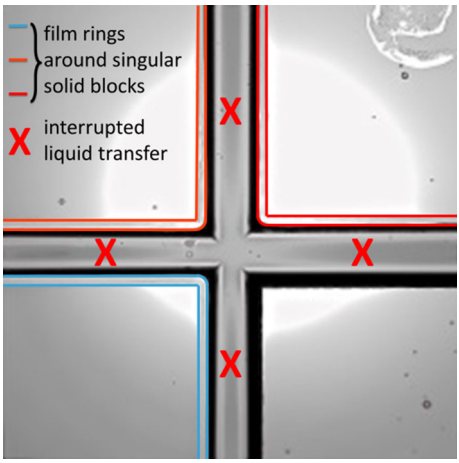

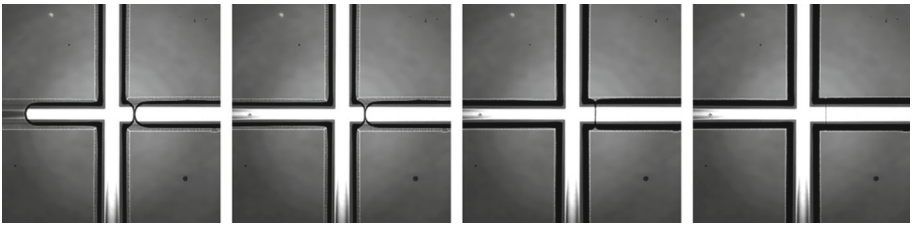

Fig. 7 Image series of a drying pore junction. Throats are interconnected by liquid bridges in the vicinity (as e.g. seen in the eastern throat), which results in simultaneous shrinking of all rings

Fig. 6, which highlights different films forming around different neighbouring solid blocks of the pore junction. It is furthermore emphasized in Fig. 6 that films are strongly assumed to be disconnected of each other, i.e. forming disconnected liquid rings around the solid, as soon as throats and the pore are completely empty and liquid bridges have disappeared. This assumption is confirmed in Fig. 5e–h which clearly demonstrate that films disappear independent of each other (at first, the south-east film dries out in Fig. 5e, and then the south-west ring dries in Fig. 5g; in Fig. 5h, all rings are dried out). Nevertheless, it was also observed that liquid rings can shrink simultaneously when connected by liquid bridges, as illustrated in Fig. 7. The tile scan in Fig. 8 shows a detail of the dry network with liquid films remaining around solid blocks connected to either a bulk meniscus (BM), single meniscus (SM) or a liquid bridge (LR) as denoted in the figure. (Dried blocks (DB) are also indicated in Fig. 8.)

The detected mean film width (before shrinkage, i.e. found usually when rings are still connected to a liquid cluster, a meniscus or a liquid bridge) was $21.4 \pm 2.4\,\mu$m. It must be noticed that the width of individual film rings could vary: (a) spatially and (b) temporally. Spatial variations, usually in the range of around 1–2 μm, are explainable by film pinning on surface elevations and depressions. Temporal variations, i.e. fluctuations of the film width, are assigned to variations in the capillary pressure threshold of the liquid cluster connected to a ring (see discussions in Sect. 3.2.2).

In summary, the CLSM experiment discussed in this section confirms the formation of capillary liquid rings as the main objects resulting from trapping of liquid in the channel

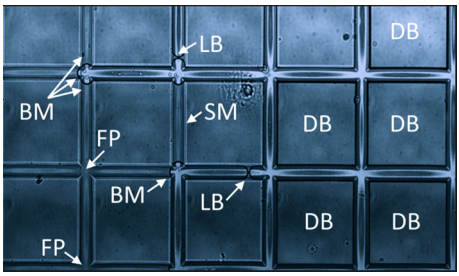

Fig. 8 A tile scan of the drying pore network shows the vicinity of pore junctions evidencing the representative phenomena occurring during the drying process: full or saturated pores (FP), empty pores (all other pores in the figure, not denoted), bulk menisci (BM), single menisci (SM), liquid bridges (LB) as well as completely dried throats (surrounding the denoted dried blocks (DB) in the figure) and throats containing liquid rings (all other throats)

corners. Additionally, however, liquid bridges between rings can form and last for a significant time period, providing possible hydraulic connectivity between rings.

3 PNM of Drying with Capillary Ring Formations

The proposed two-dimensional liquid ring model is based on the CLSM observations and the therefrom derived assumption that in the case of negligible surface roughness of the channel bottom (Fig. 4), liquid films are restricted to the corners along the edges of solid blocks as sketched in Figs. 1 and 2 and shown in Sect. 2.2. The existence of thin surface films could not be proven experimentally, and as they are furthermore of minor significance for liquid mass transfer, e.g. Laurindo and Prat (1998), thin films are disregarded in pore network modelling.

3.1 Drying PNM Without Capillary Ring Formation

The drying PNM with capillary ring formation proposed in the present paper can be regarded as an extension of the model without films, e.g. Prat (1993). In this model, capillary effects are taken into account through a simple invasion percolation rule applied to each liquid cluster present in the network: the throat emptying in a cluster is the throat of smallest capillary pressure threshold (i.e. of largest width) among the throats forming the boundary of the cluster. This rule is combined to the finite volume computation of the diffusion transport of vapour in the gaseous throats to simulate the drying process. Since this model has been presented in several previous publications, e.g. Prat (2002) and Metzger et al. (2007), the details are not repeated here. We simply recall the main features of this model with the assumptions corresponding to the version used in Vorhauer et al. (2013).

In the pore network model, the void space of porous media is represented by a two-dimensional regular square lattice of discrete pores and throats with randomly distributed size (Fig. 1). For simplicity, the cross section of throats is assumed to be rectangular and thus close to the experimental shape (Fig. 2). The distance between the centres of two adjacent pores, denoted by L, is the lattice spacing. Computational nodes are also located in the free gas above the pore network so as to include the external mass boundary layer in the computation. This is useful for a better representation of mass transfer at the open surface of the network (Irawan, Metzger and Tsotsas 2005; Surasani et al. 2008). The thickness of the external boundary layer is denoted by s_{BL}.

In drying simulations, the total void space is initially saturated with water; then evaporation starts from the open side of the network (all other sides of the network are impermeable for mass transfer). In the discrete pore network model, mass balances of individual gas and liquid throats (set of linear equations) are solved stepwise (Metzger et al. 2007). Because of the moderate evaporation rates and relatively large throats, viscosity effects in the liquid phase are disregarded in the model and liquid throats empty in the order of decreasing liquid pressure during drying (Prat 1993). Liquid transport in full ($S_{\mathrm{ij}} = 1$) and partially saturated ($0 < S_{\mathrm{ij}} < 1$) throats ij (Fig. 1) is a result of the so-called capillary pumping effect which is due to liquid pressure gradients usually existing between small throats (where the liquid pressure is lower) and large throats (where the liquid pressure is higher). As a consequence of the capillary pumping effect (when invasion is controlled by capillarity), the throat of smallest capillary invasion threshold at the periphery of a liquid cluster is assumed to be the only one invaded in the considered cluster. According to Laplace's law, the capillary invasion threshold of a throat is given by

$$P_{\mathrm{c,ij}} \approx \sigma(T_{\mathrm{ij}}) \cos\theta \left(\frac{1}{r_{\mathrm{t,ij}}} + \frac{2}{L_{\mathrm{d}}} \right) \tag{1}$$

where σ is the surface tension, $r_{t,\mathrm{ij}}$ is the throat half width and L_{d} is the throat depth. Thus, as mentioned before, this is the throat of largest width at the periphery of a cluster which is invaded as the result of evaporation.

At the gas liquid interface, local thermodynamic evaporation equilibrium with saturation vapour pressure P_v^* is assumed. Vapour transfer in the gas phase is based on vapour pressure gradients between the phase boundary (P_v^*) and the surrounding gas phase ($P_{v,\infty} = 0$), which is specified in the last pore row of the external boundary layer (Fig. 1). The mass flow rate of vapour $\dot{M}_{v,\mathrm{ij}}$ through a throat ij is computed using a linear diffusion approach taking into account the Stefan correction:

$$\dot{M}_{\mathrm{v,ij}} \approx A_{\mathrm{t,ij}} \frac{\delta(T_{\mathrm{ij}})}{L} \frac{P\tilde{M}_{\mathrm{v}}}{\tilde{R}T_{\mathrm{ij}}} \ln\left[\frac{P - P_{\mathrm{v,i}}}{P - P_{\mathrm{v,j}}} \right] \tag{2}$$

where $A_{t,\mathrm{ij}}$ is the cross-sectional area of the throat ij, δ denotes the vapour diffusion coefficient, $\tilde{M}_{\mathrm{V}}$ the molar mass of vapour, L is the lattice spacing, $\tilde{R}$ the ideal gas constant, P the total gas pressure, $P_{\mathrm{v},i}$ the vapour pressure in adjacent pore i and T_{ij} is the temperature of throat ij. As specified in detail in Vorhauer et al. (2013), temperatures vary slightly in space during experiments. Thus, the temperature field from experiment (with $62.5\,^{\circ}\mathrm{C} < T < 64.1\,^{\circ}\mathrm{C}$, $\bar{T} \sim 63\,^{\circ}\mathrm{C}$) is respected in simulations (refer to Vorhauer et al. 2013 for more details). Since temperature affects surface tension of liquid and therewith the capillary pressure, order of emptying of liquid menisci can be different when the variations are high enough (see also Vorhauer et al. 2014). At second, the saturation vapour pressure P_{V}^* is temperature depending. Due to this, vapour pressure gradients can occur at the gas liquid interface, allowing for diffusive flows between pores neighbouring liquid throat and ring menisci.

3.2 Drying PNM with Capillary Ring Formation

The consideration of capillary ring formation implies a number of model modifications (as already proposed by Wang et al. 2013, 2014). First note that the capillary bridges between rings, as shown for example in Figs. 5 or 7, are only somewhat indirectly taken into account through the partially empty throats (with $0 < S_{\mathrm{ij}} < 1$) present in the network.

3.2.1 Hydraulic Connectivity Between Liquid Regions Due to Capillary Rings

In what follows, a 'bulk meniscus' (see Fig. 1) refers to a meniscus developed over the full cross section of a channel (i.e. throat). This is the type of meniscus observed in a network of throats when corner film formation can be excluded. A 'partially developed capillary ring' denotes a system of interconnected corner films around a block when at least one channel along the block is still fully occupied by the liquid. A 'fully developed capillary ring' (also referred to as disconnected ring in Fig. 1) is a liquid ring around a block obtained when the ring has detached from the main liquid phase. Thus, in our system, a fully developed capillary ring is formed by the four corner films present along the four edges of a solid block (see Figs. 1, 9 where such a ring is called a single ring).

From CLSM measurements, we could identify that liquid rings usually dry out *after* detachment from the main liquid phase, i.e. after they had been disconnected from bulk menisci or liquid bridges (as shown in Fig. 5). Thus, we can assume that liquid corners forming a partially developed ring can interconnect the liquid phase as long as they are directly connected to at least a single bulk meniscus or a liquid bridge, i.e. a partially empty throat. Thus, a partially developed capillary ring can provide a hydraulic connection between two regions of a cluster that would be considered to be formed by two distinct clusters in the absence of the ring. In other terms, we can actually consider two options: the simplest option, cluster labelling option 1 (CLO1), consists in neglecting the intercluster hydraulic connectivity provided by the capillary liquid rings. Under these circumstances, the liquid cluster detection algorithm works as in the model without rings. This is the situation as presented in Fig. 9b. Option 2 (CLO2) consists in considering that two liquid regions connected to the same (partially developed) ring belongs to the same liquid cluster (this situation is referred to interconnected liquid clusters) (Fig. 9a). Under these circumstances, the liquid cluster

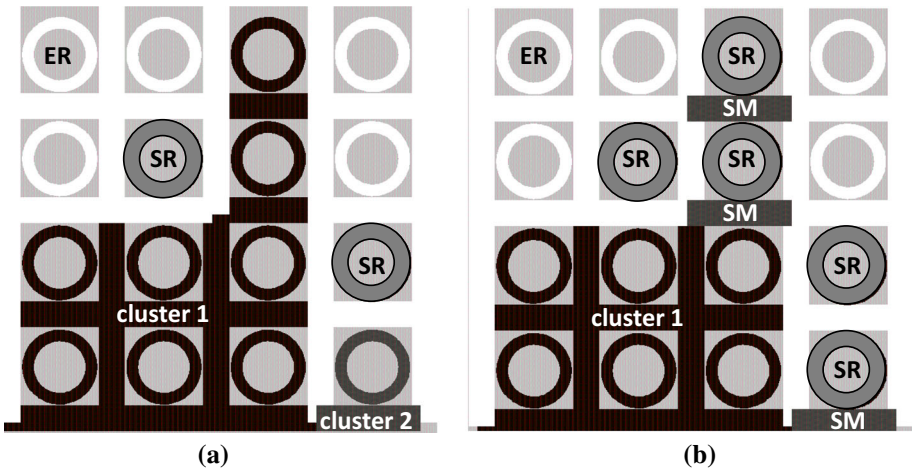

Fig. 9 Consideration of hydraulic connectivity due to capillary rings: **a** situation when it is assumed that capillary rings can act as hydraulic connectors (option CLO2). In this case, there are two liquid clusters and two isolated rings (i.e. single rings (SR)) in this example. **b** Situation when it is assumed that rings cannot act as hydraulic connectors (option CLO1). In this case, there are one main liquid cluster (smaller than the main liquid cluster in **a**), three clusters formed by a single liquid-filled throat (denoted by single meniscus (SM)) and five isolated capillary rings (SR). ER denotes empty rings. Liquid in *black*. Gas phase in *white*. Solid in *grey*

detection algorithm must be modified so as to take into account the additional hydraulic connectivity due to the presence of corner films. In contrast to the rather traditional cluster labelling algorithm as, for example, discussed in Metzger et al. (2007), which is based on the neighbour relations of liquid-filled pores, liquid rings are the basis for the cluster labelling algorithm in the novel model. Pores and throats are labelled according to their ring neighbours. More precisely, partially developed capillary rings are identified with a label higher or equal to 1, determining the label of connected bulk menisci and liquid-filled pores. Fully developed capillary rings (single rings) are indicated with label 0. Unless otherwise mentioned, we have adopted option 2 (CLO2) in agreement with the images shown in Fig. 5. A comparison between the two options is however discussed in Sect. 4.4.

3.2.2 Liquid Pressure and Liquid Volume in a Capillary Ring

The liquid pressure in a ring must vary during its formation. Similarly as for the liquid corners forming in a single square capillary (Chauvet et al. 2009), continuity of the liquid pressure is assumed between the corner film and the channel with the receding bulk meniscus found at the boundary of the liquid cluster to which also the considered partially developed ring belongs to. Using Eq. 1 and the notations shown in Fig. 2b, this can be expressed as

$$P_c \approx \sigma\,(T)\cos\theta\left(\frac{1}{r_{t,d}}+\frac{2}{L_d}\right)\approx\frac{2\sigma\,(T)\cos\theta}{h\,(L_r)}. \tag{3}$$

Thus, the capillary pressure inside a circular ring with the radius $L_r/2$ (assuming $L_r == h$) is equal to the capillary pressure of the receding bulk meniscus adjacent to the ring which is the last to be invaded by the gas phase. In this, r_{td} is the half width of the channel containing the meniscus at detachment.

Equation 3 is consistent with the experimentally observed temporal fluctuations of ring thickness since the capillary pressure fluctuates with the successive channel invasions in the cluster to which the partially developed ring is attached. Thus, the ring volume at detachment varies from one ring to the other. Although it is possible to track the various invasions leading to the formation of rings, a simpler approach was adopted. Considering the mean throat size as a good representative size, one could simply determine the half width of the ring $L_r/2$ from Eq. 3, with $r_{t,d} = \bar{r}_t$ ($\bar{r}_t \approx 82\,\mu m$). This leads to $L_r \approx 31.5\,\mu m$, which is slightly overestimating the experimentally observed mean ring width ($21.4 \pm 2.4\,\mu m$). (Deviations must be explained with the assumption of circular rings which deviates from the microscopic channel geometry of the SiO_2 network.) Naturally, an accurate theoretical determination would be much more involved, e.g. Wong et al. (1992), and must take the exact shape of the channel into account. We adopted a simple approach. In this, the volume of rings inside the pore network is computed as

$$V_r \approx 4L_r h(L-2\bar{r}_t); \tag{4}$$

however, the surface of the network is not wetted by rings (Fig. 1), so that

$$V_r \approx 3L_r h(L-2\bar{r}_t), \tag{5}$$

in rings at the top row of pore network.

Unless otherwise mentioned, we took the experimentally estimated mean ring width $L_r = 21.4\,\mu m$ in Eqs. 4 and 5 and $h == L_d = 39\,\mu m$ to estimate the ring volume at detachment. Thus, V_r is constant.

3.2.3 Liquid Cluster–Capillary Ring Mass Balance

The overall liquid saturation in a pore network without ring is computed as

$$S = \frac{\sum S_t V_t + \sum S_p V_p}{\sum V_t + \sum V_p} \tag{6}$$

where S_t is the saturation in a throat and S_p the saturation in a pore. The sums are over the total number of throats (subscript t) and pores (p) present in the network.

In the presence of rings, the overall saturation is computed similarly as

$$S = \frac{\sum S_t V_t + \sum S_p V_p + \sum S_r V_r}{\sum V_t + \sum V_p + \sum V_r} \tag{7}$$

where S_r is the saturation in a ring. The ring saturation S_r is 1 at ring formation (or more precisely ring detachment from throat menisci) and then can decrease down to zero as the result of evaporation. V_r is computed from Eqs. 4 and 5.

Of course, the mass balance between rings and liquid clusters must be satisfied properly. The volume of liquid corresponding to a ring at detachment is withdrawn from the cluster from which the ring forms.

3.2.4 Evaporation from a Capillary Ring

To compute evaporation in the network, we make the approximation that vapour pressure in a pore is equal to saturation vapour pressure when the pore is an immediate neighbour to a meniscus (throat meniscus or ring meniscus), adapted to the situation described by Wang et al. (2013, 2014). Such a pore is referred to as an interfacial pore. This assumption gives boundary conditions for the numerical computation of the vapour partial pressure field in the network. Once this vapour partial pressure field is known, the evaporation rate from an interfacial pore i is computed from the sum of vapour diffusion flow rates through adjacent empty throats,

$$\dot{M}_{v,i} = \sum \dot{M}_{v,ij} = A_{t,ij} \frac{\delta(T_{ij})}{L} \frac{P\tilde{M}_v}{\tilde{R}T_{ij}} \ln\left[\frac{P - P_{v,i}}{P - P_{v,j}}\right] \tag{8}$$

where the index j runs over all the adjacent totally empty throats transporting the vapour. Eq. 8 follows that vapour transport through empty throats ij is directly depending on the pressure gradient between the two neighbour pores i and j. With the initial definition (i.e. pores possess saturation vapour pressure when connected to a bulk meniscus or ring meniscus), it can be concluded that the pressure gradient is $\Delta P_{ij} = 0$ if the throat contains either a throat meniscus or a ring meniscus (see also Fig. 1), assuming locally constant temperatures. The evaporation rate from Eq. 8 is distributed among liquid elements (ring menisci, bulk menisci) connected to pore i. This distribution is based on the interface ratio $A_{t,ij}/A_{i,tot}$ and $A_{r,i}/A_{i,tot}$ of each element. For a bulk meniscus (typically a meniscus at the entrance of a throat), we simply define the cross-sectional area of throat $A_{t,ij}$ as the evaporation surface area. For a ring, the evaporation surface area $A_{r,i}$ is defined as

$$A_{r,i} \approx \alpha h \, (L - 2\bar{r}_t) \tag{9}$$

where the dimensionless coefficient α denotes a dimensionless constant fitting parameter introduced to specify the extent of the ring evaporation surface area (see Fig. 10 and the related discussions) and h denotes the ring height. We assumed the ring height h to be equal

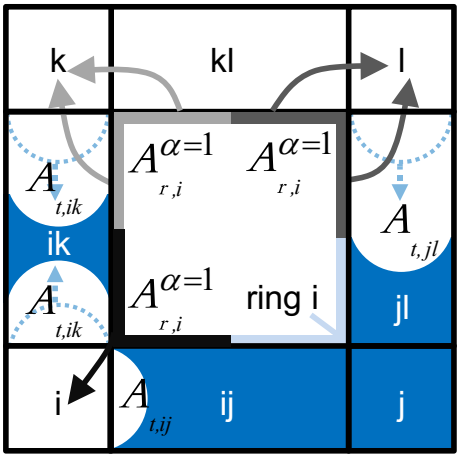

Fig. 10 Illustration of active evaporation interfaces of ring i (in *light blue*) and bulk menisci ik, jl and ij contributing to pore i, k and l, for the situation when $\alpha = 1$. The active ring interfaces are shown in *black* (pore i), *light grey* (pore k) and *dark grey* (pore l). In the algorithm with CLO2, ring i interconnects the liquid bridge in throat ik with the cluster connected to pore j. The total evaporation flow rate, for example, from pore k is computed from the sum of evaporation flow rates of ring i and the meniscus found in throat ik related to the evaporation surface areas $A_{\mathrm{r,i}}$ and $A_{\mathrm{t,ik}}$. Or rather, the evaporation flow rate from pore k is distributed among the two liquid elements directly connected to pore k

to the network depth L_d. The total evaporation surface area of neighbouring active meniscus throats and rings is computed from

$$A_{\mathrm{i,tot}} = \sum_{\mathrm{i}} A_{\mathrm{r,i}} + \sum_{\mathrm{ij}} A_{\mathrm{t,ij}}. \tag{10}$$

From this, follow the evaporation rates of neighbouring liquid bulk menisci and liquid rings:

$$\dot{M}_{\mathrm{v,tij}} \approx \frac{A_{\mathrm{t,ij}}}{A_{\mathrm{i,tot}}} \dot{M}_{\mathrm{v,i}} \tag{11}$$

$$\dot{M}_{\mathrm{v,ri}} \approx \frac{A_{\mathrm{r,i}}}{A_{\mathrm{i,tot}}} \dot{M}_{\mathrm{v,i}} \tag{12}$$

Finally, the evaporation rate of the cluster is computed from the sum of evaporation rates of all interface elements that possess identical cluster labels. The liquid element at the cluster boundary with the largest liquid pressure empties with a rate that is identical to the cluster evaporation rate. As we apply simple invasion percolation rules and neglect viscosity of the liquid phase, each cluster has exactly one moving liquid element (usually a bulk meniscus). Time stepping is determined through the emptying of one liquid element.

Note that the evaporation surface area of a ring is constant and independent of throat saturation and ring saturation in this approach. For example, the increase in evaporation surface area of rings with receding of a liquid meniscus (as illustrated in Fig. 10) could be taken into account in a future model. However, as will be explained in Sect. 4.3, the consideration of exact definition of ring evaporation surface area is assumed to have a minor impact on simulation results.

3.2.5 Algorithm of PNM with Capillary Ring Formation

The above introduced pore network model with capillary ring formation can be summarized with the following algorithm:

1. Identification of liquid clusters and single liquid elements (usually liquid rings) in the pore network.
2. Identification of throat and ring menisci at the boundary of each cluster and identification of meniscus saturations.
3. Computation of the vapour pressure field inside empty network pores and computation of the resulting diffusion flow rates through empty pore network throats.
4. Computation of evaporation rates of each liquid element at the cluster boundaries (throat menisci and ring menisci) and single liquid elements as well as computation of the accumulated cluster evaporation rates.
5. Identification of that liquid cluster element at each cluster boundary which can produce the lowest capillary pressure (usually a liquid throat meniscus). This element is referred to as the local candidate, and it contains the only moving meniscus within each cluster.
6. Computation of the time that is needed to fully empty the local candidate of each cluster at the accumulated evaporation rates computed in 4 (all other cluster menisci remain stationary) and computation of the drying time of single liquid elements.
7. Identification of the local candidate with the shortest drying time among all clusters and single liquid elements. This element is the global candidate and chosen as the one to be emptied during this time step.
8. Update of throat and ring saturations and cluster labels.

4 PNM Simulations of Drying with Capillary Ring Formation

In this section, we will show an example of typical phase distributions obtained with the PNM with capillary ring formation and briefly discuss the impact of a few parameters of the model on simulation results. The size of pore network is the same as in the experiment (thus a 50×50 pore network), and the throat size and pore size distributions are the same as the ones used to fabricate the experimental micromodel (fabrication inaccuracies are taken into account).

4.1 Phase Distribution

An example of phase distribution obtained with the PNM with capillary ring formation is shown in Fig. 11. Three main types of regions can be distinguished, namely the dry region, the liquid region and the capillary ring region, similar as in the experiment.

As can be seen, many rings can be present in the system but as expected they remain confined in the two-phase region. This is in contrast with the continuous film PNM which can predict large regions where the films are present (as illustrated in Fig. 17). This was of course expected since detached rings are not hydraulically interconnected in our model.

4.2 Impact of Ring Volumes

Figure 12 illustrates the impact of ring volume on the global drying behaviour. In Fig. 12, drying curves and drying rate curves for different initial ring volumes (= volumes at detachment), i.e. computed for $L_r = 21.4\,\mu m$ (observed mean ring width in the 2D SiO_2 pore

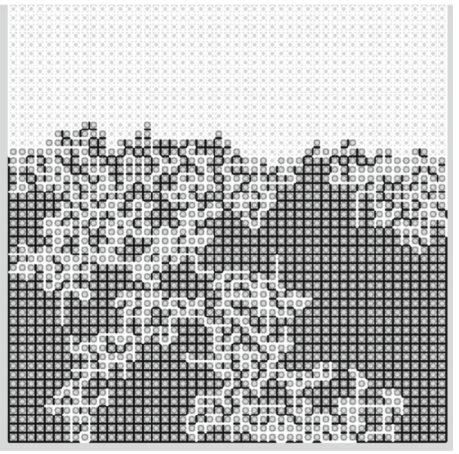

Fig. 11 Example of a phase distribution obtained with the PNM with capillary ring formation. The pores and throats fully occupied by the liquid are in *black*. The dried solid blocks are shown as *circles* surrounded by a *white ring*, whereas blocks with liquid capillary rings are shown as *circles* surrounded by a *dark grey ring*

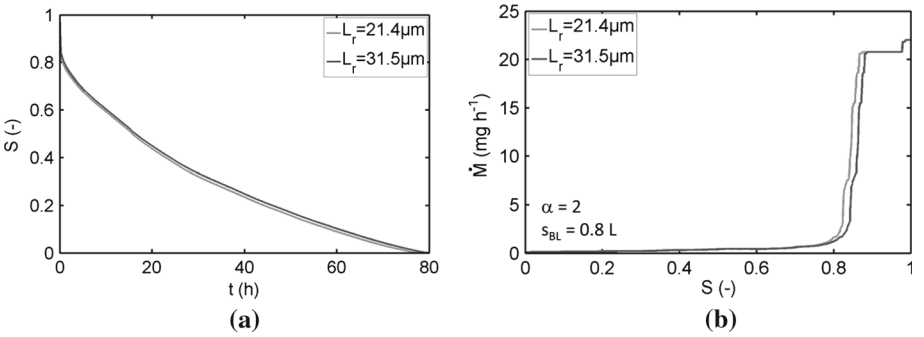

Fig. 12 Impact of ring volume: drying curves (**a**) and drying rates (**b**) for drying in the 50×50 pore network as defined above (and $\alpha = 2$, $s_{\mathrm{BL}} = 0.8L$) and different ring volumes. Drying is slightly faster in the network with smaller rings

network) and for $L_{\mathrm{r}} = 31.5\,\mu\mathrm{m}$ (estimated mean ring width), are plotted. As can be seen, the impact is moderate, but nevertheless drying appears to be faster in the case of a smaller initial ring volume. At first sight, this drying behaviour seems counter intuitive. It was additionally found that the phase distributions are almost identical in both simulations, i.e. drying front position is not affected by initial ring volume, and hence, drying rates are identical, when plotted against number of invasions (therefore the phase distributions are not shown here). However, at the beginning of drying, when rings in the first rows of blocks affect drying kinetics, liquid is drawn from throats and pores, while the majority of liquid rings remains fully saturated (in Fig. 13a saturation of rings decreases only slightly at the beginning of drying in both cases). This explains the initially constant drying rates (Fig. 12b) in the two presented simulations. During this constant rate period (CRP), more liquid is removed from the network with smaller rings in each invasion event, and hence, the overall network saturation decreases slightly faster (Fig. 13b). When rings are afterwards disconnected from the main liquid phase and start to evaporate, the drying front recedes into the network and drying rates decrease since the water vapour transfer by diffusion (from the drying front to the open network side) is very slow compared to capillary liquid pumping. This drying period is therefore denoted as the falling rate period (FRP). This is the limiting and most

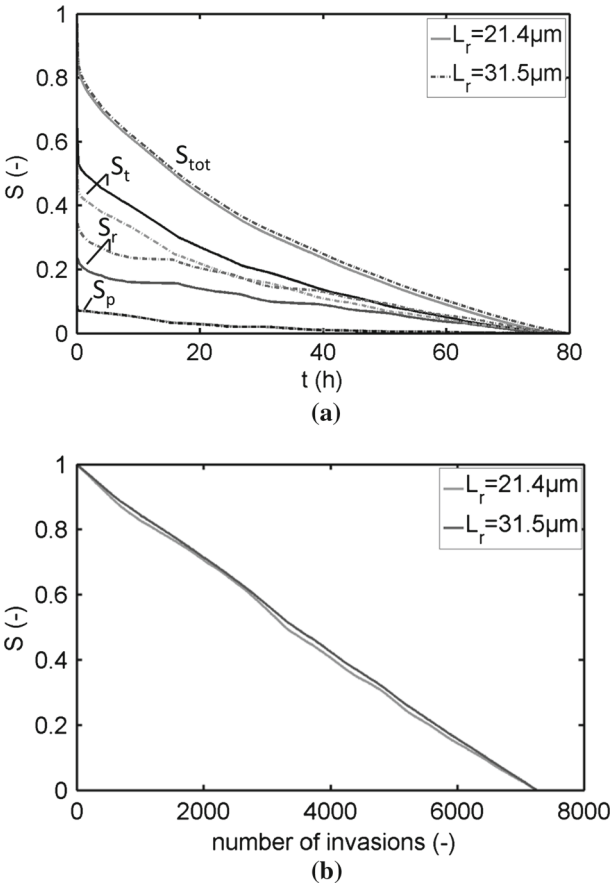

Fig. 13 Impact of ring volume: **a** total network saturation S (Eq. 7) and saturation of throats S_t, pores S_p and rings S_r over time t. Saturation of elements (throats, pores, rings) is computed from the liquid volume in elements divided by the total network volume (e.g. $S_t = \left(\sum S_t V_t\right) / \left(\sum V_t + \sum V_p + \sum V_r\right)$). **b** Decrease in overall network saturation S in each invasion event. *Solid lines* for the case $L_r = 21.4\,\mu m$ and *dashed lines* for $L_r = 31.5\,\mu m$

time consuming period during a drying process, especially in a two-dimensional system. In this period, less liquid must be evaporated from the network with smaller ring volume.

4.3 Impact of Ring Effective Evaporation Surface Area

The effective evaporation surface area of rings can be modified by means of parameter α, see Sect. 3.2.4 and Fig. 10. As described earlier, α controls the extent of the ring evaporation surface area. For example, half of the interface of a ring would physically contribute to evaporation rate in a neighbouring pore for $\alpha = 2$ (see also Fig. 10). Smaller values of α refer to a decreased ratio of the ring evaporation surface area compared to the total evaporation interface computed from the sum of cross sections of all adjacent menisci and ring interfaces. However, simulations indicate that drying time and rate are independent of the selected value for α. This behaviour seems again counter intuitive, but it can be explained from intrinsic model characteristics. It follows from Eq. 10 that the total evaporation area that is taken into

account to relate the evaporation flow rates from liquid menisci und liquid rings neighboured to a pore is computed from the sum of evaporation surface areas of adjacent menisci and ring. If the liquid phase is interconnected, per definition rings and throats belong to the same cluster; in this case, the total evaporation flow rate (of the cluster) computed in pore i is independent from α. Furthermore, as expressed by Eq. 8, diffusion flow rates depend on the pressure gradient between pore i and pore j as well as on the diffusivity inside the interconnecting throats ij (in Eq. 8 $A_{t,ij}$ denotes the cross section of already empty throats). Diffusive flow rates are independent of the total evaporation interface. However, evaporation rates of each meniscus and liquid ring depend on $A_{i,tot}$ or more precisely on the ratios $A_{t,ij}/A_{i,tot}$ and $A_{r,i}/A_{i,tot}$ (see Eqs. 11 and 12). For example, reduction in α leads to an increase in the ratio of evaporation interfaces of menisci $A_{t,ij}/A_{i,tot}$. Nevertheless, as long as rings and throats belong to the same cluster (which is a given constraint in the model with interconnection of liquid menisci by rings), the drying result is not affected.

Based on these findings, it can be assumed that a pore scale consideration of dynamics of developing ring evaporation interfaces does not affect the measureable macroscopic drying kinetics. However, as will be shown later, when we discuss the effect of interconnection of liquid by rings, the situation is different in the network without interconnection due to rings (model applying cluster labelling option 1 (CLO1)). Then, it is more apparent that neighbouring ring and menisci are disconnected and therefore higher α result in an earlier emptying of rings, while the neighbouring menisci can still contain liquid.

4.4 Impact of Hydraulic Connectivity Due to Capillary Rings

As discussed in Sect. 3.2.1, two options can be distinguished dependent on the hydraulic connectivity properties of the capillary rings. The two options, namely CLO1 and CLO2, are compared in this section. As can be seen from Fig. 14a, b, which show the phase distributions obtained from simulations with CLO2 and CLO1, respectively, at different overall network saturations S, the main liquid phase is significantly more ramified and breakthrough occurs at a higher network saturation in option CLO2 (Fig. 14a). By contrast, the liquid phase is more compact (i.e. emerging of comparably larger clusters) when interconnection is annulled in option CLO1 (Fig. 14b). As a result, drying front advances only slightly faster in the network without interconnection (Fig. 14b) resulting in a slightly earlier decrease in drying rates and an overall longer drying time (Fig. 15). The comparison with simple PNM simulations (ignoring liquid films) (Fig. 14c) shows that phase distribution as obtained for CLO1 are quite similar to phase distribution without liquid rings; concerning the drying front position, it must be noticed that it is even slightly more advanced in Fig. 14b (CLO1).

As discussed in the previous section, the impact of parameter α is of greater importance when rings and neighbouring menisci are disconnected (option CLO1). This is illustrated in Fig. 15, where the simulations with $\alpha = 2$ (solid lines in Fig. 15) are compared with one simulation with $\alpha = 0.01$ (and annulled interconnection) (dashed line in Fig. 15). Figure 15 shows that a smaller ratio of ring evaporation interface (indicated by a reduced α) and thus a higher ratio of the meniscus interface can lead to a decrease in drying time as overall drying rates are slightly increased.

5 Comparison Between Experiments and PNM Simulations

Basically, three versions of the PNM of drying are now available if we take into account the PNM with capillary ring formation presented in the present article (and Wang et al. 2013,

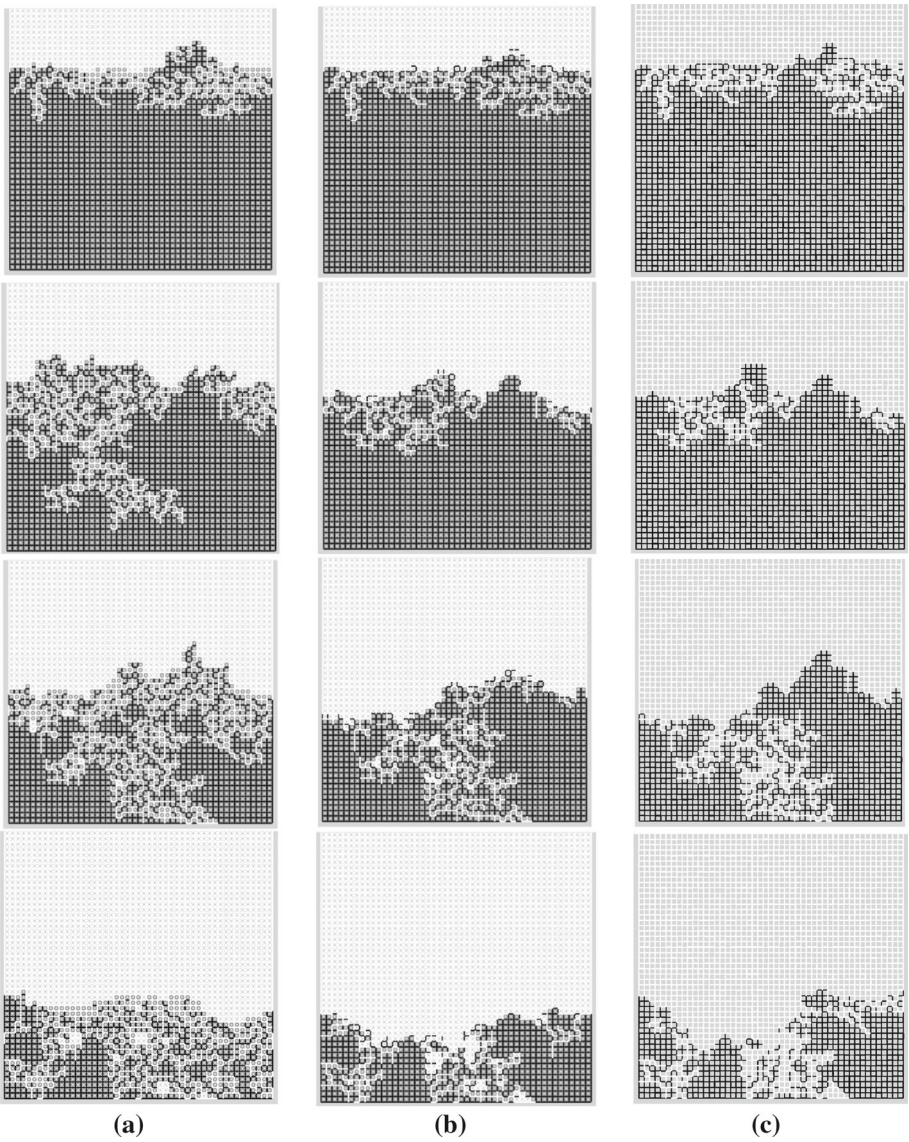

Fig. 14 Impact of ring interconnection: Phase distributions from drying with option CLO2 (i.e. taking interconnection into account) (**a**) and with option CLO1 (no interconnection of clusters by liquid rings) (**b**) at S = [0.72, 0.54, 0.38, 0.21]. Drying front position is more advanced when drying is without interconnection. Column **c** shows the phase distribution obtained with simple PNM neglecting the liquid trapping in corners

2014): the simplest model neglecting all secondary capillary effects, e.g. Prat (1993), the PNM with continuous corner films (Yiotis et al. 2003, 2004; Prat 2007) and the PNM with capillary ring formation. In the following, these models will be referred to as the simple PNM, the continuous film PNM and the capillary ring PNM, respectively. In this section, the comparisons between these three models and experimental data are presented and discussed. Note that the overall saturation in the experiment was obtained by image processing.

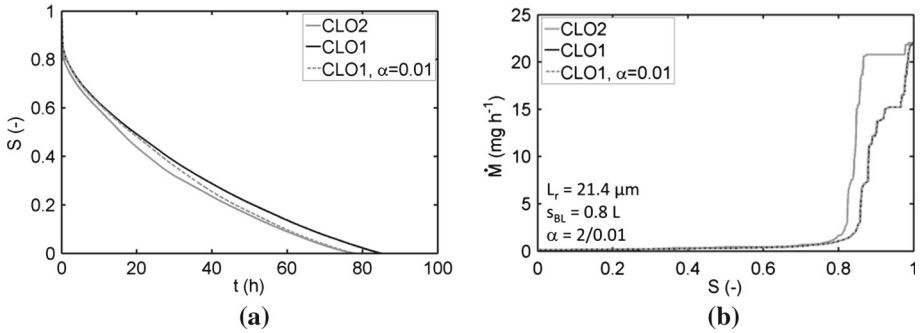

Fig. 15 Impact of ring interconnection: drying curves (**a**) and drying rates (**b**). Drying is faster when rings allow for interconnection of single menisci and separated clusters (CLO2). The *dashed grey curve* ($\alpha = 0.01$) evidences that the relation of evaporation interfaces of rings and meniscus throats is more significant when interconnection is abandoned in CLO1

5.1 Comparison of Simple PNM and Continuous Film PNM

As reported in Vorhauer et al. (2013), comparison between the experimental result and the simple PNM described in Prat (1993) was first performed. It could be shown in Vorhauer et al. (2013) that this model can lead to phase distributions strongly resembling experimental distributions. However, as illustrated in Fig. 16, drying is significantly faster in experiment compared to simulations. Nevertheless, a good agreement can be obtained using the continuous film PNM (Fig. 16) when playing with the contact angle θ as a fitting parameter. The good agreement shown in Fig. 16 was obtained for $\theta \sim 43°$ (Vorhauer et al. 2014). As discussed by Yiotis et al. (2012) and Chauvet et al. (2010), the same result might be obtained when adapting the factor of corner roundness.

Still, as illustrated in Fig. 17, the extent of the film region in simulation (grey region in Fig. 17b) is unrealistical large compared to the experiment (Fig. 17a), especially at lower overall network saturations. Thus, it is interesting to observe that the continuous film PNM already leads to a quite good agreement with the experiment in terms of evaporation rate (as illustrated in Fig. 16), whereas the physics of secondary capillary effects in the experiment is absolutely not the same as underlying in this model. In other terms, this is an excellent example where a good agreement (of drying curves) between a model and an experiment is not necessarily sufficient to conclude that the model is good. The poor agreement between the model and the experiment (in terms of phase distribution) is in fact clearly illustrated in Fig. 17.

5.2 Comparison of Simple PNM and Capillary Ring PNM

Figure 18a shows the comparison between the simple PNM, the capillary ring PNM and the experimental result. As can be seen, the simple PNM and the capillary ring PNM lead to similar results as regards the evolution of global saturation. This was expected since the rings are confined in the two-phase zone and the phase distributions obtained with the two models (see Fig. 14) are not sufficiently different to expect a significant difference in terms of drying rates (Fig. 18b). Moreover, both models significantly overpredict the drying time.

In summary, as discussed in Sect. 5.1, the continuous film PNM leads to a good agreement with the experiment as regards the drying curve (see Fig. 16) but not in terms of the spatial extent of the corner film region (as shown in Fig. 17), whereas the capillary ring PNM as

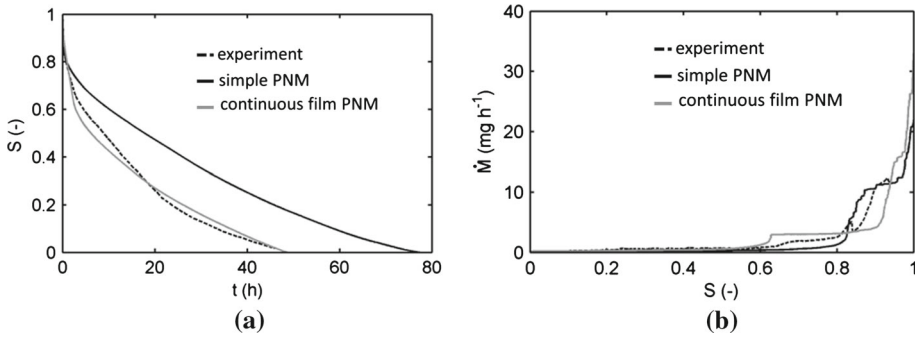

Fig. 16 Comparison between numerical pore network simulations, using the simple PNM and the continuous film PNM, and the experimental result with the SiO_2 etched network: drying curves (**a**) and drying rates (**b**) as reported in Vorhauer et al. (2014)

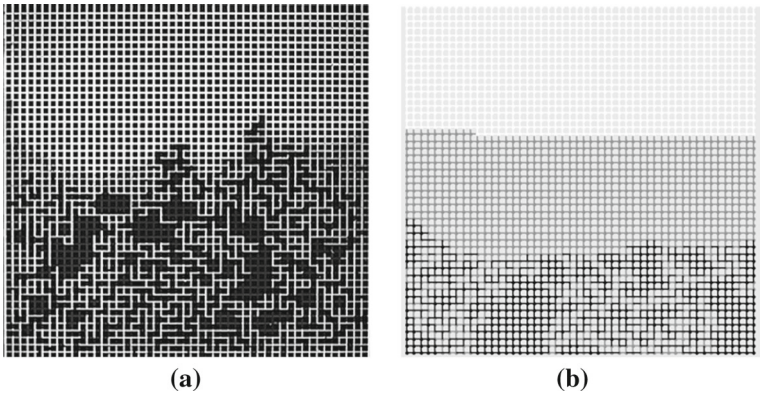

Fig. 17 Representative example of comparison between experimental (**a**) and computed (**b**) phase distribution using the continuous film PNM. The extent of the corner film region is strongly overestimated with the continuous film PNM as can be identified by the large grey region in the simulated phase distribution

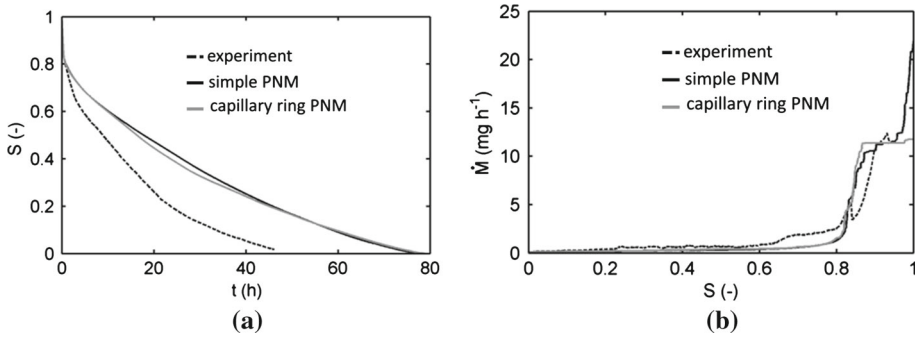

Fig. 18 Global liquid saturation as a function of time (**a**) and the therefrom derived drying rate curves (**b**). Comparison between the simple PNM, the capillary ring PNM and the experimental result with the SiO_2 etched network. The boundary layer thickness in the capillary ring model is $s_{BL} = 1.5L$

discussed in this section gives phase distributions which can be considered as the ones closest to the experimental ones (dry region, liquid region, intermediate greyscale region of similar spatial extension as in the experiment) but leads to a poor agreement in terms of drying curves (as illustrated in Fig. 18). This must be explained by edge effects, i.e. pinning of liquid at the lateral network boundaries that play a significant role in experiments, as will be discussed in the next section.

5.3 Edge Effect

When considering experimental phase distributions as shown in Fig. 3 for a comparison with PNM phase distributions as shown in Fig. 14, a striking difference lies in the lateral pinning of the liquid phase which can be observed in the experimental phase distributions (Fig. 3). This pinning, which could be provoked by continuous films covering the lateral network boundaries or by local network defects related to the fabrication process or even channel blockings, is not observed in simulations (as presented in Fig. 14). Since the evaporation flux is roughly proportional to the distance between the least advanced menisci in the network and the (top) open edge of network, it seems clear that the lateral pinning of liquid phase in the experiment, referred to as the edge effect in what follows, can explain the difference (i.e. different drying curves) between experiment and simulation.

To further explore this issue, simulations were performed so as to mimic the edge effect. A simple way of introducing a lateral pinning is to impose relatively smaller throats in the regions adjacent to the lateral edges. Since drying is essentially an invasion percolation process in the capillary limit considered in the present article, invasion of large throats is favored and therefore reduced widths of throats along the edge must delay invasion of throats by the gas phase along network edges. To investigate numerically the edge effect, radii of vertical and horizontal throats inside the two lateral columns on each side of the network were reduced by a factor 0.1. With this modification, the capillary ring PNM led to the phase distributions shown in Fig. 19, which qualitatively reproduce the edge effect as expected.

When experimental results are compared with simulated results from the capillary ring PNM in Fig. 19, it must be noticed that liquid in experimental film rings was not taken into account for computing the overall network saturation (i.e. the grey region in experimental phase distributions as shown in Fig. 19a was ignored to compute S), and thus, the actual saturation of the experimental network shown in Fig. 19a is always higher than the one deduced from image processing. Contrarily, ring saturation was taken into account to compute the overall network saturation in capillary ring PNM simulations (Figs. 19b, 20). Moreover, in simulations, liquid was removed from the contracted side channels. This means that the total amount of liquid that can at maximum be contained inside the network is lower than in a network without edge effects. Therefore, overall network saturation decreases slightly faster in each invasion event when edge effects are taken into account.

However, results are promising when we compare phase distributions (Fig. 19) and drying curves (Fig. 20a) from experiment with those obtained from the capillary ring PNM including interconnection of liquid phase and edge effects as well as slight temperature variations (as monitored during drying experiment). When the boundary layer thickness is adapted so as to allow for capturing the initial experimental drying rate at $S_0 = 0.94$ (this value is related to the start of experimental drying curve in Fig. 20), which was estimated with $s_{BL} = 1450\,\mu m$, drying rates are overestimated during the first period of drying (Fig. 20b). This is associated with the existence of interconnecting liquid rings that could connect the liquid phase with the open network side at the beginning of drying resulting in a comparably long first drying period with constant drying rates (CRP) simulated with the capillary ring PNM. Contrarily,

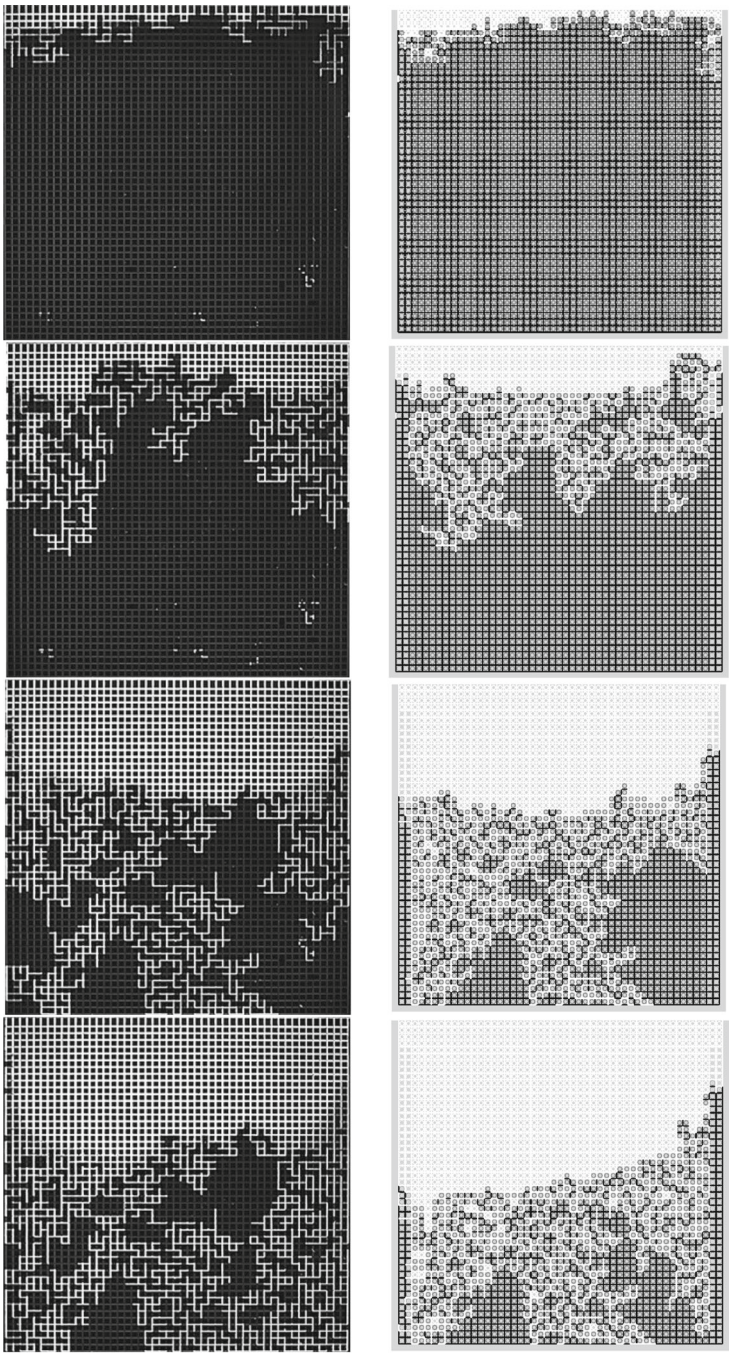

Fig. 19 Phase distributions (at $S_0 = 0.94$ and $S = [0.72, 0.40, 0.30]$) from drying experiment (**a**) and drying simulation (**b**). Simulation was with interconnected film rings of width $L_r = 21.4\,\mu m$, $\alpha = 2$, $s_{BL} = 600\,\mu m$, including edge effects, temperature variations and initial saturation of $S_0 = 0.94$

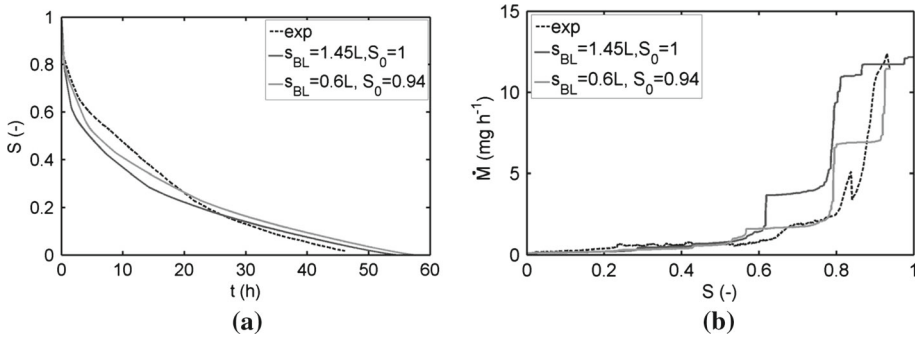

Fig. 20 Drying curves (**a**) and rates (**b**) from experiment and simulations with consideration of ring and edge effects. Simulation was with interconnected film rings of width $L_r = 21.4\,\mu m$, $\alpha = 2$, $s_{BL} = 600\,\mu m$, including edge effects, temperature variations and initial saturation of $S_0 = 0.94$

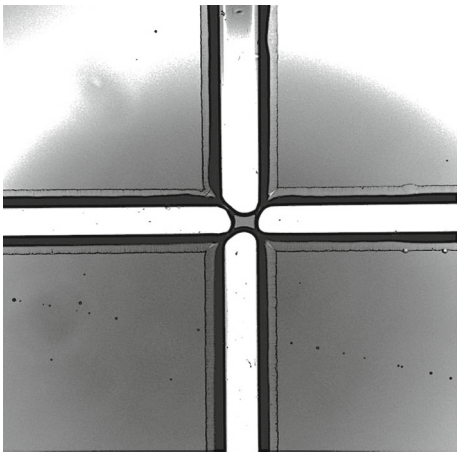

Fig. 21 Partly saturated pore junction in the vicinity of already empty throats that contain liquid film rings

a CRP could not be monitored during experimental drying; instead, drying rates dropped immediately when monitoring started (at already decreased S, $S_0 = 0.94$). At this time, liquid rings could mainly not be observed inside upper rows of the pore network (top rows in Fig. 19a). But when we respected the initial dry zone of the experimental pore network in our simulations (as depicted in Fig. 19b) and if we furthermore removed rings inside these upper dry rows, then the initially observed drying rates could partly be captured (when $s_{BL} = 600\,\mu m$) (solid light grey curve in Fig. 20b).

5.4 Discussion

Although the capillary ring PNM model led to the best agreement with the experiment for both, the structure of phase distributions and the drying curve, among the three models tested, the agreement is not excellent. One problem is the edge effect, which cannot be reliably explained and somewhat hampered the comparison. Other sources of discrepancies might lie in discrete events that are not considered by the present pore network model. As shown in Figs. 5 and 7, liquid bridges form in throats during drying of the experimental pore network. These bridges are only partially taken into account in the model through the partially empty

throats with $0 < S_{ij} < 1$. Furthermore, as illustrated in Fig. 21, liquid bridges can form inside pores. This phenomenon is neglected in all PNM simulations. All types of bridges might maintain a generally higher liquid connectivity than considered by the capillary ring PNM.

This illustrates the subtlety when concerning secondary capillary effects, even in the simple pore space geometry of a 2D system with rectangular throats as considered here.

6 Conclusions

When we compared pore network simulations with experimental drying of a 2D-etched SiO_2 pore network with non-cylindrical throats, we found that experiments are almost twice as fast as numerically predicted using a PNM neglecting corner liquid trapping, although boundary layer thickness was adapted so that initial drying rates could be captured. Based on previous works, the discrepancy could be expected to be explained with the existence of liquid films, which could be identified in experimental phase distributions. Consequently, we applied the pore network model accounting for film flow proposed in previous works (Yiotis et al. 2003, 2004; Prat 2007). We found that drying curves and rates could satisfactory be predicted when playing with the contact angle between liquid and solid, but the extent of the film region was highly overestimated. However, it was noted that the least advanced point of the film region agreed with the position of liquid-filled throats and pores at the network lateral boundaries, while the drying front penetrated the network at a significantly advanced front position in the centre of the pore network. This observation led to the consideration of edge effects as discussed in Sect. 5.3.

In this paper, we showed by means of images from confocal laser scanning microscopy (CLSM) that the assumption of continuous liquid films was indeed inadequate for drying in our SiO_2 pore network. A continuous system of films was not observed by CLSM. The observations rather indicated the formation of discrete capillary liquid rings. This led to the development of a new version of a PNM for drying, precisely a PNM with capillary ring formations. This model led to the most satisfactory comparison with experiment for both, phase distribution and drying curve, provided that the edge effect as discussed above is taken into account. The spatial extent of rings is only of one pore row. As discussed before, a similar film extent could also be obtained with the continuous film model when fitting either the contact angle or the factor that accounts for the corner roundness. However, the continuous film model does not account for the intercluster connection which is instead captured with the ring model. This leads to differences in the phase patterns between the ring model and the continuous film model.

From this, we can conclude that the pore network model with capillary ring formation can be considered as a step towards the modelling of secondary capillary effects in drying in more complex geometries such as a random packing of particles for example. Such a model has already been implemented by Wang and co-authors and is already envisioned for a future publication.

Although the capillary ring formation has a minor significance in the face of edge effects occurring in our experiment and thus the impact on drying curve and most apparent features of phase distributions is negligible compared to the edge effect, the consideration of capillary rings in drying can nevertheless be important in situations where the liquid phase contains particles or dissolved salt for example. Exemplarily, in the presence of salt, capillary rings are special locations where crystallization will take place as a result of ring evaporation. Since

the capillary rings are likely to form in the contact regions between grains, they might play a role in damages induced by the crystallization process, see, for instance, Schrerer (2004) for a presentation of this issue.

Acknowledgments The Si-SiO_2 pore network was produced by the Institute of Micro and Sensor Technique at Otto-von-Guericke University. Financial support by Deutsch-Franzoesische Hochschule (DFH-UFA) and DFG (in the frame of GKmm 1554) is gratefully acknowledged. Furthermore, the authors gratefully acknowledge the funding of part of the experimental equipment (CLSM) by the German Federal Ministry of Science and Education (BMBF) as part of the InnoProfile-Transfer project NaWiTec (03IPT701X).

References

Chauvet, F., Duru, P., Geoffroy, S., Prat, M.: Three periods of drying of a single square capillary tube. Phys. Rev. Lett. **103**, 124502 (2009)

Chauvet, F., Duru, P., Prat, M.: Depinning of evaporating liquid films in square capillary tubes: influence of corners roundness. Phys. Fluids **22**, 112113 (2010)

Geoffroy, S., Prat, M.: A review of drying theory and modelling approaches. In: Delgado, J.M.P.Q. (ed.) Chap. 7 in Drying and Wetting of Building Materials and Components, Building Pathology and Rehabilitation 4. Springer International, Switzerland (2014)

Irawan, A., Metzger, T., Tsotsas, E.: Pore network modelling of drying: combination with a boundary layer model to capture the first drying period. In: Proceedings of 7th World Congress of Chemical Engineering, Glasgow, Scotland, 10–14 July 2005

Laurindo, J.B., Prat, M.: Numerical and experimental network study of evaporation in capillary porous media: phase distributions. Chem. Eng. Sci. **51**, 5171–5185 (1996)

Laurindo, J.B., Prat, M.: Numerical and experimental network study of evaporation in capillary porous media: drying rates. Chem. Eng. Sci. **53**, 2257–2269 (1998)

Lenormand, R., Zarcone, C., Sarr, A.: Mechanisms of the displacement of one fluid by another in a network of capillary ducts. J. Fluid Mech. **135**, 337–353 (1983)

Lenormand, R., Zarcone, C.: Role of roughness and edges during imbibition in square capillaries. SPE 13264, presented at the 59th annual technical conference and exhibition of the society of petroleum engineers, Houston, 16–19 Sept 1984

Mahmood, H.T.: Modelling of liquid film rings by three-dimensional pore network drying model. Master Thesis at Otto-von-Guericke University Magdeburg (2013)

Metzger, T., Tsotsas, E., Prat, M.: Pore-network models: a powerful tool to study drying at the pore level and understand the influence of structure on drying kinetics. In: Tsotsas, E., Mujumdar, A.S. (eds.) Modern Drying Technology, Vol. 1: Computational Tools at Different Scales, pp. 57–102. Wiley-VCH, Weinheim (2007)

Prat, M.: Percolation model of drying under isothermal conditions in porous media. Int. J. Multiph. Flow **19**, 691–704 (1993)

Prat, M.: Recent advances in pore-scale models for drying of porous media. Chem. Eng. J. **86**, 153–164 (2002)

Prat, M.: On the influence of pore shape, contact angle and film flows on drying of capillary porous media. Int. J. Heat Mass Transf. **50**, 1455–1468 (2007)

Prat, M.: Pore network models of drying, contact angle and films flows. Chem. Eng. Technol. **34**, 1029–1038 (2011)

Scheel, M., Seemann, R., Brinkmann, M., DiMichiel, M., Sheppard, A., Herminghaus, S.: Liquid distribution and cohesion in wet granular assemblies beyond the capillary bridge regime. J. Phys. Condens. Matter **20**, 494236 (2008)

Schrerer, G.W.: Stress from crystallization of salt. Cem. Concr. Res. **34**, 1613–1624 (2004)

Surasani, V.K., Metzger, T., Tsotsas, E.: Influence of heating mode on drying behavior of capillary porous media: pore scale modelling. Chem. Eng. Sci. **63**, 5218–5228 (2008)

Tsimpanogiannis, I.N., Yortsos, Y.C., Poulou, S., Kanellopoulos, N., Stubos, A.K.: Scaling theory of drying in porous media. Phys. Rev. E **59**, 4353–4365 (1999)

Vorhauer, N., Tran, Q.T., Metzger, T., Tsotsas, E., Prat, M.: Experimental investigation of drying in a model porous medium: influence of thermal gradients. Dry. Technol. **31**, 920–929 (2013)

Vorhauer, N., Tsotsas, E., Prat, M.: Isothermal drying in the presence of capillary liquid films—comparison of experiments with pore network simulations in a model system. In: Proceedings of the 19th International Drying Symposium (IDS 2014), Lyon, France, 24–27 Aug 2014

Wang, Y.J., Kharaghani, A., Tsotsas, E.: Pore-scale visualization and simulation of liquid films for drying particle packing. In: Proceedings of Eurodrying, Paris, France, 2–4 Oct 2013

Wang, Y.J., Mahmood, H.T., Kharaghani, A., Tsotsas, E.: Visualization and modeling of liquid film rings observed during drying of particle packings. In: Proceedings of the 19th International Drying Symposium (IDS 2014), Lyon, France, 24–27 Aug 2014

Wong, H., Morris, S., Radke, C.J.: Three-dimensional menisci in polygonal capillaries. J. Colloid Interface Sci. **148**, 17 (1992)

Yiotis, A.G., Boudouvis, A.G., Stubos, A.K., Tsimpanogiannis, L.N., Yortsos, I.N., Yortsos, Y.C.: Effect of liquid films on the isothermal drying of porous media. Phys. Rev. E **68**, 037303 (2003)

Yiotis, A.G., Boudouvis, A.G., Stubos, A.K., Tsimpanogiannis, I.N., Yortsos, Y.C.: Effect of liquid films on the drying of porous media. AIChE J. **50**, 2721–2731 (2004)

Yiotis, A.G., Salin, D., Tajer, E.S., Yortsos, Y.C.: Drying in porous media with gravity-stabilized fronts: experimental results. Phys. Rev. E **86**, 026310 (2012)